nature water

Article

https://doi.org/10.1038/s44221-026-00690-1

Plasmon-enhanced reductive defluorination of PFAS in water under ambient conditions

Received: 8 December 2025

Accepted: 1 July 2026

Published online: 1 September 2026

Check for updates

Ozce Durak[1,4], Seung Soo S. Lee[1,4], Lydia MacFarlane Watt[1], Susanna K. Maisto[1], Fabian Menges[2], Changwoo Kim[3], James M. Mayer[2] & John D. Fortner[1]

Photo-driven, plasmon-enhanced catalysis enables polyfluoroalkyl and perfluoroalkyl substance (PFAS) degradation in water under ambient conditions. Here we show that ultraviolet (UV) irradiation-induced localized surface plasmon resonance drives reductive defluorination of perfluorooctanoic acid and perfluorooctane sulfonic acid, two legacy contaminants. Stable, quantum-sized palladium and platinum nanocatalysts supported on aminated mesoporous silica nanoparticles (MSN–NH_2–Pd and MSN–NH_2–Pt) transform perfluorooctanoic acid and perfluorooctane sulfonic acid with stoichiometric, or near-stoichiometric, fluoride release under low-intensity UVC or UVA irradiation at room temperature. Time-resolved ^{19}F nuclear magnetic resonance, high-resolution mass spectrometry and complementary analyses indicate a stepwise reductive hydrodefluorination pathway in which oxidized, short-chain products do not measurably accumulate under the conditions studied. Scavenger and control experiments are consistent with hydrated electrons and in situ hydrogen generation as key reactive species. Taken together, the results indicate that synergistic interfacial PFAS sorption, plasmon-induced hydrogen evolution and hydrated electron formation drive PFAS defluorination under mild reaction conditions.

Polyfluoroalkyl and perfluoroalkyl substances (PFAS) represent a broad class of synthetic organic chemicals that contain a hydrophobic fluorinated carbon chain and a polar end group. Due to their amphiphilic properties and high stability, PFAS have been extensively used as surface coatings, and aqueous film-forming foams for fire suppression, among other widespread applications[1], resulting in extensive environmental contamination[2]. Based on the highly recalcitrant nature of PFAS attributed to the strength of C–F covalent bonds (~485 kJ mol^{-1}) and a large number of potential PFAS structures (~15,000) occurring at low environmental concentrations with documented human health risks, effective PFAS remediation remains an important and urgent global health need[3,4], which is reflected in recent regulatory actions[5].

The treatment of PFAS contamination using conventional processes poses several challenges due to their highly stable chemical structure(s)[6]. The various technologies currently available to transform PFAS can be generally categorized as chemical/catalytic, plasma-based, thermal and bio-based[6,7]. Among these, chemical/catalytic transformation processes have proven effective for PFAS degradation via chemical oxidation and reduction, photocatalysis, electrocatalysis and sonolysis-based pathways[6]. Catalytic transformations have been demonstrated for a library of PFAS compounds with relatively lower energy/economic requirements compared with traditional methods, such as thermal degradation, and are characterized by rapid processes, unlike the slow (or limited) nature of biologically driven transformations[8,9].

From a sustainability perspective, photo-driven catalytic processes offer inherent advantages by reducing energy demands and chemical inputs. Recent advances in ultraviolet (UV) reactor design and light-emitting diode (LED) technology have significantly improved

[1]Department of Chemical and Environmental Engineering, Yale University, New Haven, CT, USA. [2]Department of Chemistry, Yale University, New Haven, CT, USA. [3]Department of Environment and Energy Engineering, Gwangju Institute of Science and Technology, Gwangju, Republic of Korea. [4]These authors contributed equally: Ozce Durak, Seung Soo S. Lee. e-mail: john.fortner@yale.edu

https://doi.org/10.1038/s44221-026-00690-1

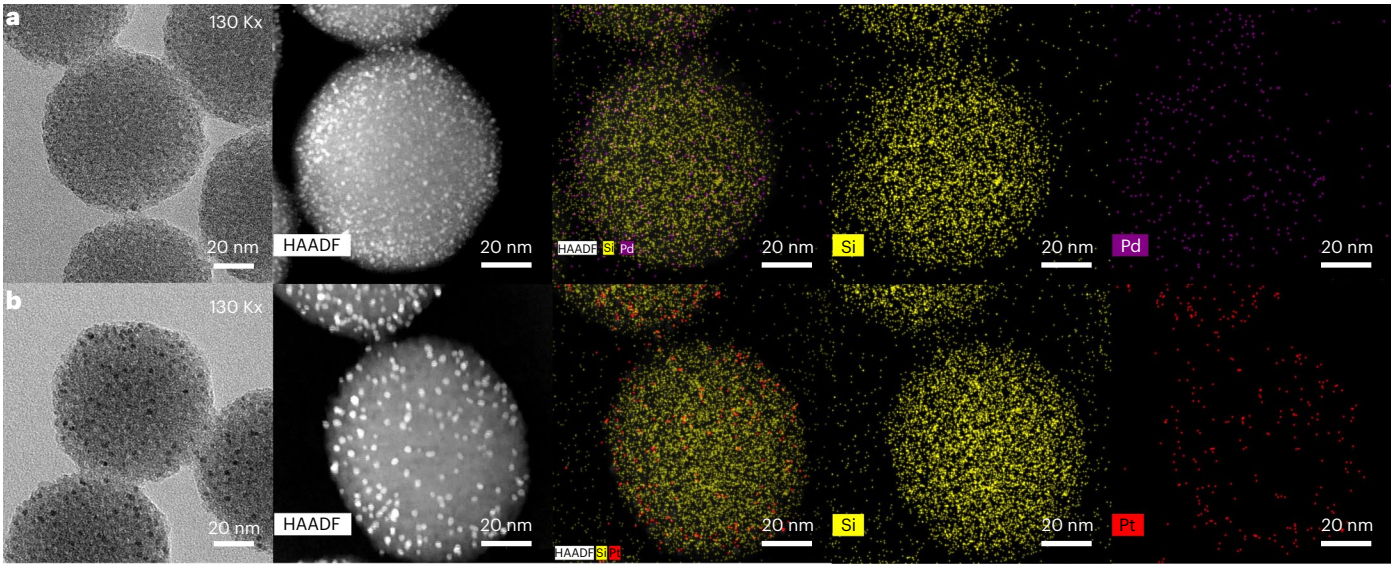


Fig. 1 | Structural and elemental characterization of Pd- and Pt-loaded MSN. a,**b**, TEM, high-angle annular dark-field scanning TEM (HAADF-STEM) and corresponding EDS elemental maps of MSN–NH_2–Pd (**a**) and MSN–NH_2–Pt (**b**), showing uniform dispersion of metal nanoparticles supported on MSN. Kx represents 1,000 times magnification.

the scalability and energy efficiency of UV-based treatment systems, making them increasingly viable for scaled water treatment and environmental remediation[10,11]. Techno-economic analyses have further highlighted the potential cost-effectiveness of UV-driven approaches, particularly for decentralized or point-of-entry treatment scenarios compared with other emerging technologies[12,13]. Among photocatalytic strategies, plasmon-enhanced photocatalysis, a growing field focused on enabling/enhancing chemical reactions through specific light–matter interactions, is a powerful strategy for driving thermodynamically challenging reactions under ambient conditions[14]. This approach exploits localized surface plasmon resonance (LSPR), which arises from the photoexcitation of free electrons in metal nanostructures, typically noble metal nanoparticles (for example, Au, Ag, Pd and Pt), in the 0.5–8 nm size range[15]. When incident light matches the plasmon resonance frequency, collective oscillation of surface electrons is induced, generating highly energetic charge carriers ('hot' electrons and holes), localized heating and/or strong electromagnetic fields at the nanoparticle interface[16]. Such light-induced processes have been harnessed to catalyse a range of chemical transformations, including hydrogen evolution via water splitting, selective hydrogenation reactions and degradation of environmental pollutants[17–21]. However, while clear potential exists, this approach has not been demonstrated for effective PFAS treatment, despite supportive computational reports[22,23].

In this study, plasmon-induced, photocatalytic defluorination of PFAS is demonstrated through an efficient, reductive mechanism, with minimal inputs at room temperature (RT). For this, stable LSPR-active palladium (Pd) and platinum (Pt) catalysts supported on mesoporous silica nanoparticles (MSN) were developed and demonstrated under UV irradiation (both UVC and UVA). For optimized materials and conditions, we observe near-stochiometric (~100%) defluorination for both perfluorooctanoic acid (PFOA) and perfluorooctane sulfonic acid (PFOS), with (similarly) high reaction kinetics and no external hydrogen required. Reaction pathway(s) are explored and described through control experiments and advanced, time-resolved spectroscopic analyses.

Results and discussion

Synthesis and characterization of plasmonic photocatalysts

MSN holds significant potential as a material platform(s) for environmental applications based on facile/scalable synthesis, (surface) functional and geometric tunability, and stability. As demonstrated by our lab and others, such properties also make MSN an ideal candidate for supporting/stabilizing metal nanoparticle deposition and, thus, a catalyst(s) support for reaction-based applications[24]. In this study, synthesized MSN support particles were highly porous, monodisperse, spherical structures with an average particle size of 77.7 ± 6.1 nm (Supplementary Fig. 1) with high surface area (496.3 $m^2 g^{-1}$) and an average pore diameter of 3.6 nm (Supplementary Fig. 2).

To facilitate metal nanoparticle deposition, MSN was surface functionalized with primary amine groups (MSN–NH_2), and subsequent metal (Pd and Pt) nanoparticle synthesis/deposition, was carried out under solvothermal conditions as detailed in Supplementary Information. The average particle sizes of monodispersed Pd and Pt nanoparticles on MSN-NH_2 were determined to be 0.7 ± 0.1 nm and 1.5 ± 0.9 nm (Fig. 1a,b), which is consistent with small-angle X-ray scattering measurements presented in Supplementary Fig. 2. For materials evaluated, metal nanoparticle concentrations on MSN–NH_2, were 4.0 wt% for Pd and 3.7 wt% for Pt. Additional characterization of both plasmonic photocatalysts including X-ray diffraction (crystal structure) and X-ray photoelectron spectroscopy (elemental oxidation states and relative ratios) can be found in our previous study[25].

Plasmonic nanoparticles (PNPs), including Pd and Pt, can catalyse various reactions through three primary energy dissipation mechanisms: heat generation, enhancement of the electric field, and/or hot electron formation[26]. For this, the energy of the photon is transferred into the oscillating surface free electrons and subsequently excites a resonance mode that can be identified with response(s) in the reflected light intensity via absorption-sensitive diffuse reflectance spectroscopy (DRS)[27]. Consistent with previous studies, MSN–NH_2 support material has relatively low optical absorption in the UV–visible (UV–vis) region, between the wavelengths of 800 nm and 200 nm, allowing LSPR absorption bands of associated Pd and Pt PNPs (termed MSN–NH_2–Pd and MSN–NH_2–Pt) to be observed in the 370–250 nm range[27] (Supplementary Fig. 3). Accordingly, aqueous reactions were conducted under constant UVC or UVA irradiation as discussed below. We note that PNP stability was also evaluated after reaction (up to 96 h) with Pd/Pt PNPs remaining highly stable throughout, with no evidence surface-based particle aggregation (via time-resolved transmission electron microscopy (TEM) analysis) or particle dissolution (inductively coupled plasma mass spectrometry (ICP-MS) analysis).

https://doi.org/10.1038/s44221-026-00690-1

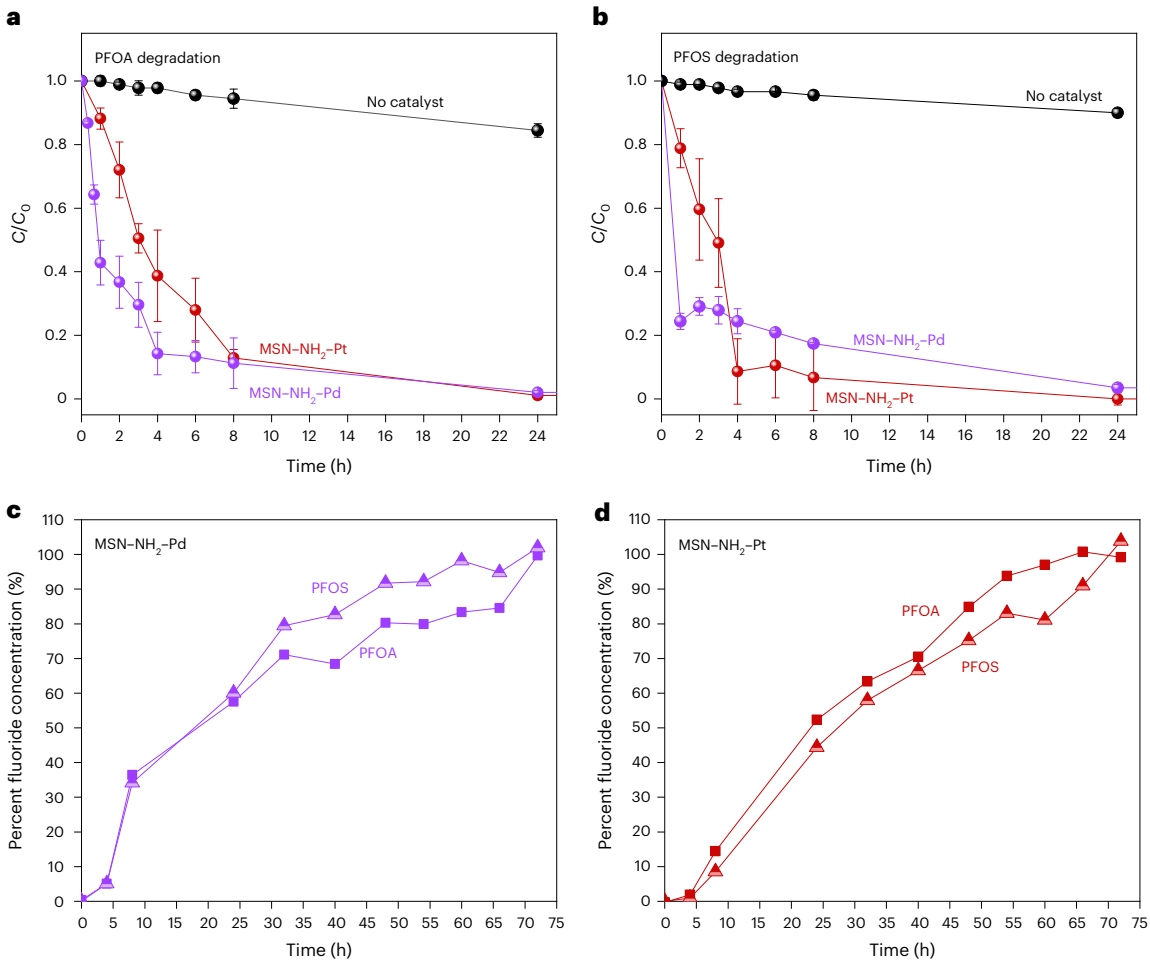


Fig. 2 | Plasmonic photocatalyst-driven reductive defluorination of PFOA and PFOS. a,**b**, Metal-dependent defluorination of PFOA (**a**) and PFOS (**b**) using MSN–NH_2–Pd and MSN–NH_2–Pt under constant UVC irradiation with 20 ppm MeOH ($^{\bullet}$OH scavenger) and CO_2 at pH 4.2–4.5 over 24 h. In no-catalyst control experiments conducted under studied conditions, no measurable fluoride formation was observed over time, indicating that direct photolysis of PFOA or PFOS under constant UVC irradiation does not promote reductive defluorination. **c**,**d**, Percent fluoride release (quantified via IC) over 72 h for MSN–NH_2–Pd (**c**) and MSN–NH_2–Pt (**d**) during PFOA and PFOS degradation under identical conditions (as in **a** and **b**). All experiments used 10 ppm PFAS (quantified via LC–MS) and 400 ppm photocatalyst (40 mg). Data are presented as mean values ± s.d., and error bars represent the standard deviation (s.d., $n = 3$, n derived from different experimental samples).

Reductive PFAS transformation

As-synthesized PNPs supported on MSN–NH_2 (MSN–NH_2–Pd and MSN–NH_2–Pt) were evaluated for PFAS transformation, under a matrix of reaction conditions. For this, we focused on two environmentally relevant, commonly found (and studied) eight-carbon chain PFAS compounds, PFOA and PFOS, representing two PFAS classes (carboxylic acid and sulfonic acid). The experimental design was structured to control key reaction parameters, including pH, light irradiation conditions, and potential radicals/reactive species (thus appropriate scavengers). Both MSN–NH_2–Pd and MSN–NH_2–Pt completely degraded PFOA and PFOS, as shown in Fig. 2a,b, under constant UVC irradiation (light intensity of 2.6 mW cm^{-2}), in the presence of a hydroxyl scavenger (MeOH) at a working pH of 4.2–4.5 (achieved by CO_2 sparging/headspace). Within 24 h, MSN–NH_2–Pd (MSN–NH_2–Pt) materials (400 ppm) degraded 99.1% (99%) and 98.7% (99.9%) of PFOA and PFOS (10 ppm initial concentrations), with first-order reaction rates of 0.34 (0.25) h^{-1} and 0.27 (0.37) h^{-1}, respectively (Supplementary Table 3). In no-catalyst controls under UVC irradiation, no measurable fluoride formation was observed over time, indicating that direct photolysis does not promote reductive defluorination of either PFOA or PFOS under the conditions studied. Under the same reaction conditions, defluorination was verified via F^- mass balance using ion chromatography (IC), with near 100% defluorination efficiency for both PFOA and PFOS within 72 h (Fig. 2c,d), which was further confirmed by ^{19}F nuclear magnetic resonance (NMR) analysis (Fig. 3 and Supplementary Fig. 5). The parent PFAS degradation rate was significantly faster than the total defluorination rate as products/fragments continue to react, consistent with previous studies[28,29]. Enhanced reaction rates and degradation extent in the presence of hydroxyl radical ($^{\bullet}$OH) scavenger suggest a major degradation mechanism occurs through a reductive reaction pathway (Supplementary Fig. 4). Observed defluorination efficiencies are comparable to those reported for several reductive PFAS defluorination systems in the literature, which span a broad range depending on catalyst composition and reaction conditions[28–35].

PFAS defluorination via advanced reductive processes (ARP) offers advantages over oxidative pathways, which often produce shorter-chain PFAS (for example, PFHpA, PFHxA, PFPeA and PFBA) that are generally more hydrophilic, less well understood and subject to evolving regulatory requirements[28,29,34–38]. Furthermore, common aqueous-based oxidative species (for example, hydroxyl radicals and superoxide radicals) do not efficiently react with C–F bonds unless used in some combination with additional conditions/reactive species, such as sulfate radical-based oxidation ($SO_4^{\bullet-}$)[39,40]. It has also been shown theoretically that reductive degradation requires comparatively

https://doi.org/10.1038/s44221-026-00690-1

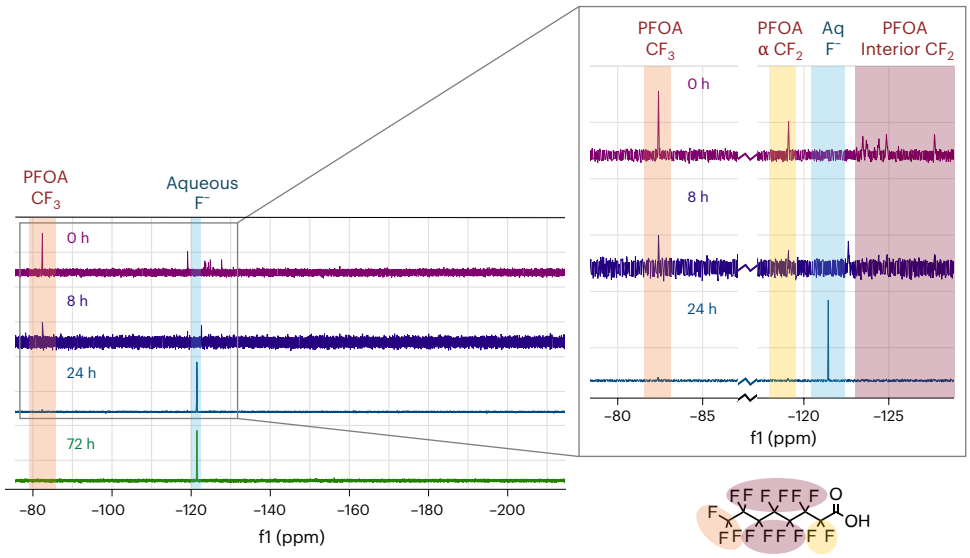


Fig. 3 | Time-resolved liquid-state ^{19}F NMR analysis of reductive defluorination. Spectra show aliquots collected during PFOA degradation with MSN–NH_2–Pd under constant UVC irradiation in the presence of MeOH and CO_2 at pH 4.2–4.5 over 72 h. The inset includes an axis break between −85 ppm and −117 ppm for clarity and f1 (*x* axis) represents frequency dimension. As the reaction proceeds, signals corresponding to PFOA decrease, while those associated with aqueous fluoride (F^-) increase. The 0 h spectrum displays 7 characteristic PFOA peaks, including CF_3 (−82.40 ppm) and α-CF_2 (−119.10 ppm) signals. At 72 h, PFOA signals are no longer observed, and a relatively intense F^- signal emerges at −121.44 ppm, supporting IC (fluoride evolution) measurements. Detailed methodology and peak assignments are provided in Supplementary Information.

lower energy (compared with other treatment processes), making it a more cost-effective and scalable solution[41,42].

Assessing major reaction variables

Reaction parameters, including pH, reactive species and incident light were explored through a matrix of control experiments, which are summarized in Supplementary Table 3. For reactions evaluating pH and reactive species, MSN–NH_2–Pd was used as the plasmonic photocatalyst and PFOA as the target PFAS. The role of pH was assessed by applying CO_2 headspace to maintain mildly acidic conditions (pH 4.2–4.5), deionized (DI) water for circumneutral pH (pH 6.8–7.2) and a bicarbonate buffer (pH 9.2) for mildly basic conditions. For these, we observe higher performance under acidic conditions (continuous UVC irradiation with MeOH) as shown in Fig. 4a, which aligns with a surface-sorption model for more (effectively) positively charged surfaces as depicted in Supplementary Fig. 6, and by others[43]. Batch PFAS sorption isotherm measurements conducted within this pH range, presented in Supplementary Table 4 and Supplementary Fig. 7, show favourable PFAS sorption under evaluated conditions. Catalyst suspensions kept in the dark (Fig. 4b and Supplementary Fig. 8) showed no measurable fluoride formation over time, confirming that irradiation is required.

Reactivity was also evaluated under UVA irradiation (λ = 368 nm, light intensity of 7.3 mW cm^{-2}). For these experiments, PFOA degradation efficiency decreased from 99.1% to 60.7% for MSN–NH_2–Pd while MSN–NH_2–Pt decreased from 99% to 69.8% (Fig. 4b and Supplementary Fig. 8) for a 24-h reaction period. Similar efficiency trends are observed for PFOS degradation (Supplementary Fig. 9). While slower than UVC-based reactions, MSN–NH_2–Pd also catalyse reductive defluorination of both PFOA and PFOS upon UVA irradiation, with corresponding fluoride evolution observed (~80% fluoride evolution for both PFOA and PFOS over a 96-h reaction time; Supplementary Fig. 10). By contrast, MSN–NH_2–Pt did not achieve similar defluorination outcomes either PFAS. To compare (photo)efficiency of different UV wavelengths (that is, UVA versus UVC), photon flux normalized reaction rates are presented in Supplementary Table 5. For PFOA, MSN–NH_2–Pd and MSN–NH_2–Pt show the highest per-photon efficiency (1.1×10^{-20} h^{-1} and 0.8×10^{-20} h^{-1} per applied photon, respectively) under UVC. UVA-based reactions under identical conditions were comparatively less efficient, with normalized rates of 6×10^{-22} h^{-1} and 2×10^{-22} h^{-1} per applied photon, respectively. Considering PFOS defluorination, MSN–NH_2–Pd and MSN–NH_2–Pt under UVC also exhibit similar normalized rates (0.8×10^{-20} h^{-1} and 1.1×10^{-20} h^{-1} per applied photon, respectively). UVA-based PFOS defluorination reactions, were observed to decrease similar to PFOA (8×10^{-22} h^{-1} and 2×10^{-22} h^{-1} per applied photon for MSN–NH_2–Pd and MSN–NH_2–Pt, respectively). Collectively, UVC offers a clear advantage in per-photon efficiency (~10–75×) for all materials and PFAS evaluated, despite the higher incident photon flux under UVA. This is consistent with higher photon energy and more favourable absorption within the UVC range (for example, 254 nm) for both Pd and Pt metals (Supplementary Fig. 3). However, UVA-based defluorination processes do have the distinct advantage of being compatible with solar or near-visible LED sources that are typically more cost-effective and longer-lived than traditional UVC lamps[44]. Furthermore, while proof of concept of UVA-based reductive defluorination is achieved here for MSN–NH_2–Pd, material improvements towards more plasmonic-based efficient (for example, UVA, solar and visible light) reactions are likely to be achieved in the future[45,46].

Identifying major reactive species

As briefly discussed, the presence of $^{\bullet}$OH scavenger increased reaction kinetics (Supplementary Fig. 4), while the degradation efficiency of PFOA (within 24 h) decreased to 65.3% (from 99.1% with MeOH under identical experimental conditions) in the absence of a hydroxyl scavenger[43] (here MeOH, *tert*-butanol (TBA) or isopropanol (IPA) were evaluated; Supplementary Fig. 4). This suggests that an oxidative pathway probably competes with the reductive pathway[47,48], which is further supported by liquid chromatography–mass spectrometry (LC–MS) analysis, whereby chain-shortened PFCA (for PFOA degradation) by-products are observed when no scavenger is present (Supplementary Fig. 11).

Reactive species involved in the reductive pathway were further explored using appropriate scavengers in excess. For this, $AgNO_3$ was used to scavenge reducing species[30,49,50], such as hydrated electrons (e_{aq}^-), whereas superoxide dismutase (SOD) and ethylenediaminetetraacetic acid (EDTA) were used to scavenge, superoxide radical ($O_2^{\bullet-}$),

https://doi.org/10.1038/s44221-026-00690-1

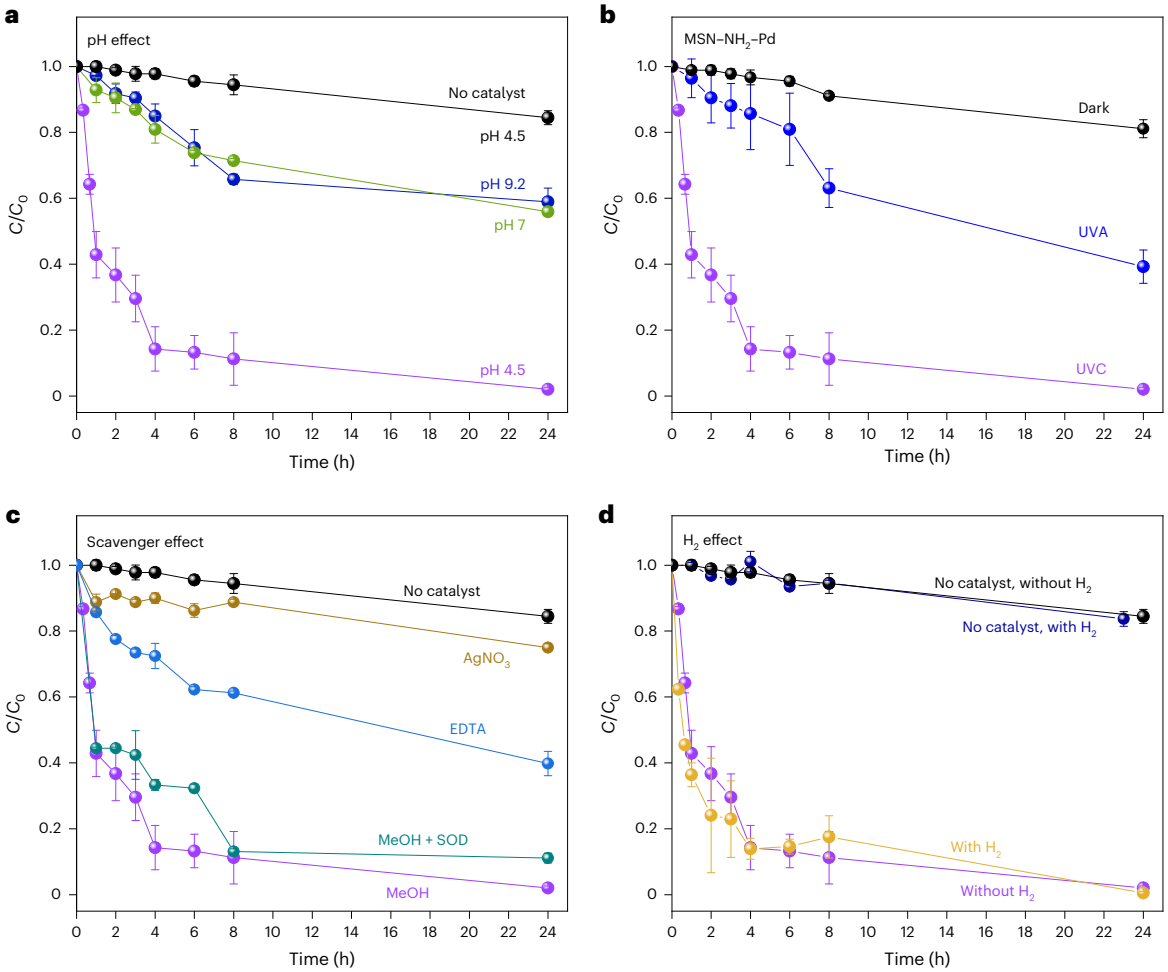


Fig. 4 | Reaction conditions affecting PFOA transformation. a, pH-dependent performance of MSN–NH_2–Pd particle under constant UVC irradiation with 20 ppm MeOH and no applied H_2. **b**, Light-dependent performance of plasmonic photocatalyst MSN–NH_2–Pd for PFOA degradation under constant UVC/A irradiation with 20 ppm MeOH and applied CO_2 (pH 4.2–4.5). Catalyst suspensions kept in the dark showed no measurable fluoride formation over time, indicating that UVC or UVA irradiation is required for reductive PFAS degradation to proceed. **c**, Scavenger-dependent performance of MSN–NH_2–Pd particle under constant UVC irradiation with applied CO_2 (pH 4.2–4.5) and no external H_2. **d**, H_2-dependent performance of MSN–NH_2–Pd under constant UVC irradiation with 20 ppm MeOH and applied CO_2 (pH 4.2–4.5). All experiments used 10 ppm PFOA quantified via LC–MS, with 400 ppm catalyst (40 mg MSN–NH_2–Pd or MSN–NH_2–Pt) over 24 h. Data are presented as mean values ± s.d., and error bars represent the standard deviation (s.d., $n = 3$, n derived from different experimental samples).

and holes (h^+), respectively. Formation reactions of reactive species are given below, in equations (1)–(4)[51,52]. It is noteworthy that, given equation (2) and the reported pK_a of the $H^\bullet/e_{aq}^-$ redox couple, $H_{aq}^\bullet$ is not expected to be present under our experimental conditions.

$$[Pd_n]^0 + h\nu \rightarrow [Pd_n]^{+1} + e_{aq}^- \quad (1)$$

$$e_{aq}^- + H^+ \rightarrow H^\bullet \quad (2)$$

$$e_{aq}^- + O_2 \rightarrow O_2^{\bullet -} \quad (3)$$

$$h^+ + H_2O \rightarrow x^\bullet OH + H^+ \quad (4)$$

Considering PFOA degradation, data presented in Fig. 4c indicate that $O_2^{\bullet -}$ and h^+ play low(er) or negligible roles in the observed reaction process. By contrast, e_{aq}^- appears to be a primary reactive species, as demonstrated by the dramatic decrease in degradation performance with $AgNO_3$ (from 99.1% to 25%, under constant UVC irradiation at 4.2–4.5 pH for 24 h) under identical reaction conditions. In the presence of $AgNO_3$, degradation performance significantly decreased, consistent with scavenging of hydrated electrons by Ag^+ and NO_3^- ($k = 2.8 \times 10^9$ and 9.7×10^9 M^{-1} s^{-1}, respectively, for reaction with e_{aq}^-)[30,49,50,52]. Although some contribution from surface effects cannot be excluded, this result, together with wavelength dependence, fluoride evolution and product distributions, supports hydrated electrons as the dominant reductive intermediate under the conditions studied. ICP-MS analysis of post-reaction solutions showed no measurable Pd or Pt dissolution, further indicating that the loss of reactivity is unlikely to arise from catalyst instability. While the precise nature of hydrated electrons remains a topic of discussion, their subsequent reaction mechanism is conventionally defined as outer sphere one-electron transfer (reduction), capable of tunnelling over long distances without requiring direct coordination[53]. The negative charge of the formed/available hot electrons polarize nearby neutral water molecules (meta)stabilizing regions that an electron can briefly occupy, also referred to as the cavity model[54]. Although hot-carrier relaxation occurs on femtosecond-to-picosecond timescales, these carriers can initiate electron ejection into water, generating hydrated electrons that persist long enough to participate in solution-phase reduction chemistry[14,55]. This phenomenon enables

https://doi.org/10.1038/s44221-026-00690-1

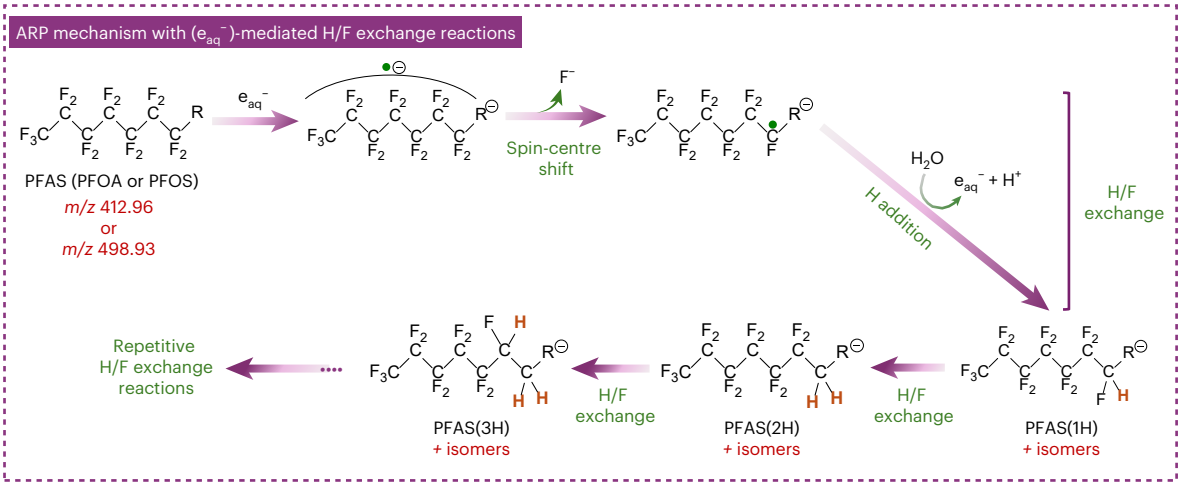


Fig. 5 | Proposed advanced reduction reaction pathway (ARP) for e_{aq}^--mediated reductive transformation of PFAS. Upon UV activation, hydrated electrons initiate C–F bond cleavage, forming a carbon-centred radical. Subsequent proton and electron additions result in stepwise H/F exchange reactions. This mechanism is consistent with ARP-type hydrohalogenation pathways and supported by HR-MS detection of partially defluorinated intermediates ($C_7F_{15-n}H_nCOO^-$ and $C_8F_{16-n}H_nSO_3^-$) as well as radical scavenger experiments. Fluoride elimination can occur from various carbon sites, generating structural isomers, with products capable of re-entering the cycle for continued H/F substitutions.

effective interaction with electronically stabilized substrates such as fluorine-saturated carbon chains[54].

LSPR-driven hydrogen generation

Conventional reductive defluorination strategies typically rely on exogenous hydrogen sources and metal catalysts to activate C–F bonds at reactive surfaces[56]. By contrast, plasmon-enhanced systems offer a fundamentally distinct approach wherein LSPR excitation can drive in situ hydrogen generation directly at the catalyst–solution interface[57,58]. This mechanism not only reduces the need for external reductants but also enables interfacial co-localization of reactants. For the plasmonic nanocatalysts evaluated, gas chromatography analysis confirmed the generation of hydrogen gas upon UV irradiation, in both the presence and the absence of PFAS upon UV irradiation (Supplementary Fig. 12). Proposed pathways for such hydrogen formation are illustrated in Supplementary Fig. 13 and discussed in detail in Supplementary Information. To assess whether hydrogen availability limits PFAS reaction kinetics, control experiments with external hydrogen gas addition were conducted, which showed nearly identical kinetics (Fig. 4d and Supplementary Table 3), indicating a self-sustaining pathway where hydrogen is not rate-limiting under the tested conditions (see the Supplementary Information for details). Importantly, in the absence of UV irradiation with external hydrogen present (sparged), significant PFAS degradation was not observed, further confirming an LSPR-driven reaction process (Supplementary Fig. 14).

PFAS reductive degradation products and pathway(s)

A detailed, time-resolved analysis of PFOA and PFOS transformation products was performed using LC–high-resolution (HR) tandem mass spectrometry (MS/MS) under conditions optimized for degradation performance[30,42] (UVC irradiation (λ = 254 nm), 400 ppm of MSN–NH_2–Pd catalyst, 10 ppm PFAS, 20 ppm MeOH (as a hydroxyl radical scavenger) and continuous CO_2 sparging to maintain mildly acidic conditions; Figs. 2 and 4). For these conditions, the primary observed products were hydrodefluorinated analogues of PFOA and PFOS that maintained their corresponding head group functionalities. This is consistent with a dominant hydrogenation-driven defluorination mechanism that does not involve significant early-stage decarboxylation or desulfonation. Considering major intermediate species, the initial carboxylate/sulfonate reaction product has one F replaced by H, $C_7F_{14}HCOO^-$ (*m/z* 394.97; Supplementary Figs. 15–20 and Supplementary Table 6) and $C_8F_{16}HSO_3^-$ (*m/z* 480.93; Supplementary Figs. 21 and 22 and Supplementary Table 7), termed PFOA(1H) or PFOS(1H). These species were transformed within the first 12 h of irradiation, and a series of more highly defluorinated products appeared over time, up to $C_7F_1H_{14}COO^-$ (14H; Supplementary Figs. 18 and 19) and $C_8H_{17}SO_3^-$ (17H; Supplementary Fig. 21), in line with a stepwise hydrodefluorination pathway and consistent with ARP mechanism, as discussed below, and corroborated by scavenger experiments (Fig. 4c and Supplementary Fig. 4). Although occurring at significantly lower abundance, we also observed decarboxylated and desulfonated products, including the perfluoroalkyl species $C_6F_{13}CF_2^-$ (*m/z* 368.97) and shorter-chain sulfonated compounds (Supplementary Figs. 15–17 and 22, and Supplementary Tables 6 and 7). The formation of these minor products indicates that alternative and simultaneous degradation pathways exist, which are probably influenced by structural differences between PFAS compounds, such as variations in head groups or surface interaction sterics and/or sites. However, these pathways appear less favourable, either kinetically or thermodynamically, under the reaction conditions used in this study.

To further explore major product structures and fragmentation behaviour, MS/MS analysis was performed to differentiate resulting isomers based on bond stability and fragmentation pathways (Supplementary Figs. 20 and 22). As the reaction proceeds, *n*H products (where *n* indicates the number of fluorine-to-hydrogen substitutions) emerge sequentially, with species exhibiting decreasing (maximum) MS signal intensities with increasing *n*. This reflects the evolution of a complex and increasingly dilute product mixture. LC traces revealed significant isomeric diversity within each *n*H class. For example, PFOA(1H) eluted in at least four major chromatographic fractions (Supplementary Figs. 17 and 18), each representing one or more positional isomers. If fluorine loss can occur from any backbone carbon, as suggested by the MS/MS data, a 2H species could produce up to 7 unique regioisomers (plus diastereomers), and at least 13 distinct 1H/2H species could coexist. As defluorination continues past 2H species, the number of possible structural isomers increases exponentially in chemical diversity, consistent with the observation of reduced occurrence of individual intermediate species. These results are in contrast to the common reports that the α-CF_2 adjacent to the carboxylate (central $-CF_2-$ segments in the case of sulfonated PFAS) is the most reactive for the first H/F exchange[29,42]. Prior computational work has

suggested that the initial dissociation site can be variable rather than restricted to a single preferred position, because the excess electron is initially delocalized over the PFAS molecule[59]. While bond dissociation energies have been proposed to assess and predict C–F bond cleavage selectivity[42], additional factors probably contribute, including PFAS association dynamics, related steric interactions and solvation of departing F^- anions.

Notably, the intermediate products observed during PFOA and PFOS degradation did not show measurable accumulation of chain-shortened carboxylate products, such as PFHpA ($C_6F_{13}COO^-$) and PFHxA ($C_5F_{11}COO^-$), by either quantitative LC–MS or LC–HR-MS/MS under the conditions studied. Shorter-chain PFCA products are typically observed via oxidative pathways, especially through a decarboxylation–hydroxylation–elimination–hydrolysis (DHEH)-based mechanism (Supplementary Fig. 23), which includes decarboxylation or desulfonation, hydroxylation, elimination and subsequent hydrolysis. In this work, the absence (or quenching) of an available oxidative reactant (for example, hydroxyl radicals) limits the hydroxylation step of DHEH process, thus inhibiting the generation of PFCA products.

ARP is well established as a pathway for PFAS transformation and is typically initiated by electron donors such as hydrated electrons, zero-valent metals or molecular hydrogen[42]. While several recent studies have explored hybrid or combined oxidative–reductive systems for PFAS treatment[28,40], relatively few have focused exclusively on ARP-based pathways operating under ambient or mild conditions and even fewer have achieved near-complete defluorination under such conditions[27,28,50,51,60]. Here, based on our experimental findings, we propose that the primary degradation pathway in this LSPR-driven system proceeds through an ARP mechanism. Specifically, LSPR excitation promotes hydrated-electron generation, which drives reductive PFAS defluorination. The process is initiated by electron transfer to the PFAS lowest unoccupied molecular orbital (LUMO), which has substantial contributions from C–F antibonding (σ^*) orbitals[61]. Such electron addition initiates F^- dissociation, leaving a fluorocarbon radical that is subsequently reduced and protonated to hydrofluorocarboxylates or hydrofluorosulfonates. This cycle is repeated to generate subsequent $C_7F_{15-n}H_nCOO^-$ or $C_8F_{16-n}H_nSO_3^-$ species, as observed (this mechanism is depicted in Fig. 5 and Supplementary Figs. 15–22). While our findings provide clear evidence for a classic ARP mechanism, future studies are needed to resolve subtle process details. For example, given the small (~3.6 nm) pores of MSN–NH_2, PFAS molecules may associate in close proximity to Pd or Pt nanoparticles (0.7–1.0 nm) with varying orientations. In such confined environments, the initial reduction step could involve hydrated electrons and/or H atoms associated with the Pd (or Pt) PNPs, either in driving C–F bond cleavage and/or in subsequent H addition to the carbon radical. Addressing these and other next-step mechanistic questions will enable deeper understanding towards optimizing light-driven, plasmonic processes for PFAS transformation.

Conclusion

This study presents a plasmon-enhanced approach for the reductive defluorination of PFOA and PFOS in aqueous media under ambient conditions. By leveraging quantum-sized Pd and Pt nanoparticles precisely dispersed on amine-functionalized mesoporous silica, we demonstrate rapid PFAS degradation kinetics and at- or near-stoichiometric defluorination upon simple UV irradiation, without the need for external hydrogen addition. Mechanistic experiments and LC–HR-MS/MS analyses of intermediate species reveal sequential H/F exchange driven primarily by hydrated electrons generated through plasmon-enabled processes.

Beyond the observed reactivity, the system offers several practical features relevant to future process development. Material synthesis is straightforward and conducted under ambient conditions using readily available precursors. The estimated raw material cost is approximately US$3.80 per gram of catalyst (Supplementary Table 8), although this value reflects raw material inputs only and excludes operating and irradiation costs, which should be incorporated in a full techno-economic assessment. The noble metals are present at lower loadings (4.0 wt% Pd and 3.7 wt% Pt on MSN–NH_2) within the composite catalyst and operate catalytically rather than stoichiometrically. ICP-MS analysis of post-reaction samples showed no measurable Pd or Pt leaching under the tested conditions, indicating catalyst stability. Reducing noble-metal content and evaluating earth-abundant alternatives will be important for future process development. The process was also effective under both UVC and UVA irradiation, suggesting compatibility with alternative light sources in future studies. Taken together, these findings establish a plasmon-enabled reductive pathway for PFAS defluorination under ambient conditions. Continued mechanistic investigation, development of visible-light-responsive variants and integration into continuous-flow systems will be important next steps towards process optimization and application.

Methods

Materials

Cetyltrimethylammonium bromide (CTAB, >99.0%), tetraethyl orthosilicate (TEOS, 98%) triethanolamine (TEA, >99.0%), (aminopropyl)triethoxysilane (APTES, 99%), chloroplatinic acid hydrate ($H_2PtCl_4{\cdot}xH_2O$, >99.9%), sodium tetrachloropalladate (Na_2PdCl_4, 99.99%), trisodium citrate dihydrate (US Pharmacopeia grade), sodium borohydride ($NaBH_4$, 99%), silver nitrate ($AgNO_3$, >99.0%), PFOA (>95.0%), superoxide dismutase (SOD, >95.0%), ethylenediaminetetraacetic acid (EDTA, >99.0%), *tert*-butyl alcohol (TBA, anhydrous, ≥99.5%), isopropyl alcohol (IPA, ≥99.5%), methanol (MeOH, 99.95%) and ethanol (EtOH, 200 proof, anhydrous, 99.5%) were purchased from Sigma-Aldrich. PFOS (>99.0%) was purchased from TCI. All experiments were conducted in ultrapure Milli-Q water (MQ water, 18.2 MΩ cm) using quartz reactors.

Synthesis of MSN supports

CTAB (5.72 g, 15.69 mmol) was dissolved in EtOH (18 g, 0.39 mol) and water (129.6 g, 7.2 mol) under stirring (750 rpm) at RT for 30 min. In the CTAB micelle-containing solution, TEA (0.568 g, 3.81 mmol) was added at RT and agitated for an additional 30 min. The final pH was recorded as approximately 9.0 ± 0.5 at RT. The mixture was then heated to 70 °C (ramp rate of 10 °C min^{-1}) under vigorous agitation (at 750 rpm). Then, TEOS (66.28 mmol) was injected into the solution at the injection rate of 1,000 µl min^{-1}, and the whole mixture was continuously stirred at 750 rpm and 70 °C for 2 h under N_2 flow. The resulting cloudy solution was further purified using HCl-containing EtOH (1.0 wt.% HCl in EtOH) and separated by centrifugation (at 13,750*g* for 25 min). The purified MSN was dried and kept under vacuum overnight. The as-synthesized MSN was further purified under acidic conditions at a high temperature above 70 °C to remove CTAB and TEA within the MSN pore space. Then, 4,000 mg of MSN was homogenously dispersed in HCl-containing EtOH (120 ml) at pH below 1.0 (typically 2 wt% HCl in EtOH) and agitated at 70 °C for 3 h. The purified MSN was cooled and separated by centrifugation (13,750*g* for 40 min). The CTAB removal process was repeated three times[62]. As synthesized, MSN exhibits a significantly larger surface area compared to nanoscale silica prepared by the Stöber method, a conventional approach, which has a Brunauer–Emmett–Teller (BET) surface area of 34.9 m^2 g^{-1} for particle sizes of approximately 200 nm, as reported elsewhere[63].

MSN amine surface modification (MSN–NH_2)

Primary amine functionalization on MSN was achieved via post-synthesis surface modification with APTES. Before the reaction, MSN samples were purified under acidic conditions to remove CTAB and TEA as described above. APTES (6 ml, 25.64 mmol) was added to the purified MSN (1,000 mg) containing EtOH/water (120 ml/60 ml) co-solvent at RT under vigorous agitation (at 750 rpm) and heated to 70 °C (ramp rate of 10 °C min^{-1}). The reaction mixture was stirred at 70 °C for 2 h under N_2 flow. The resulting cloudy solution was purified

using EtOH and separated by centrifugation (at 13,750*g* for 25 min) and stored in an amber bottle.

Palladium nanoparticles on MSN (MSN–NH_2–Pd)

Palladium nanoparticles were nucleated and grown on primary amine functionalized MSN (MSN–NH_2) in aqueous media at 83 °C. All synthetic conditions were processed using palladium and citrate stock solutions; the palladium stock solution was 0.59 mol l^{-1}, and the citrate stock solution was 0.105 mol l^{-1} (in water). The stock solutions were prepared 1 day before the reaction and stored in the refrigerator (3–5 °C). Typically, to synthesize 5 wt% Pd-loaded MSN–NH_2–Pd, 400 mg of MSN–NH_2 was dispersed in DI water (100 ml) at RT and stirred at 750 rpm under N_2 flow for 30 min. Homogeneously mixed MSN–NH_2 solution was then agitated with palladium stock solution (0.377 ml, 19.30 mg of Pd, 0.181 mmol) and sodium citrate stock solution (8.8 ml, 0.924 mmol) at RT. The temperature of the reaction was then heated to 83 °C (ramp rate of 10 °C min^{-1}) and kept at that temperature for the desired time (25, 60 and 120 min) under N_2 flow. After the reaction occurred at 83 °C, the reaction vessel was cooled immediately in an ice bath to stop the growth of Pd nanoparticles. The resulting brown precipitates (or grey/black, depending on Pd nanoparticle size and/or concentration) were purified using EtOH and water mixture, then separated by centrifugation at 13,750*g* for 25 min. The purified MSN–NH_2–Pd particles were vacuum-dried overnight and kept in an amber vial.

Platinum nanoparticles on MSN (MSN–NH_2–Pt)

Platinum nanoparticles were nucleated and grown on MSN–NH_2 in aqueous media at 90 °C. All synthetic conditions were processed using platinum and citrate stock solutions; the platinum stock solution was 0.50 mol l^{-1}, and the citrate stock solution was 0.105 mol l^{-1} (in water). The stock solutions were made 1 day before the reaction and stored in a refrigerator (3–5 °C). Typically, to make 3.7 wt% Pt-loaded MSN–Pt, 400 mg of MSN–NH_2 was dispersed in DI water (100 ml) at RT and stirred at 750 rpm under N_2 flow for 30 min. Homogeneously mixed MSN–NH_2 solution was then agitated with platinum stock solution (0.715 ml, 31.00 mg of Pt, 0.159 mmol) and sodium citrate stock solution (6.6 ml, 0.693 mmol) at RT. The reaction temperature of the reaction was then heated to 95 °C (ramp rate of 10 °C min^{-1}) and kept at that temperature for the desired time (25, 60 and 120 min) under N_2 flow. After the reaction at 90 °C, the reaction vessel was cooled immediately in an ice bath to stop the growth of Pt nanoparticles. The resulting yellow precipitates (or grey/black, depending on Pt nanoparticle size and/or concentration) were purified using EtOH and water, then separated by centrifugation at 13,750*g* for 25 min. The purified MSN–NH_2–Pt was vacuum-dried overnight and kept in an amber vial.

Characterization

As-synthesized materials were characterized through established and standard methods including TEM, ICP-MS, UV–vis DRS and BET surface area analyser. The size and shape of the engineered nanomaterials was characterized through FEI Tecnai Osiris 200 KV TEM. TEM samples (10 mg of sample in 10 ml of EtOH) were bath-sonicated for several minutes, and a drop of the dispersed sample was subsequently placed onto a TEM grid and left to dry overnight at RT under ambient air. The elemental composition analysis of the nanomaterials was examined by ICP-MS (NexION 5000, PerkinElmer) to determine the metal loading and nanoparticle integrity/dissolution (throughout 0–72 h experimental time frame) of the plasmonic photocatalysts. The analytical samples were digested in the boiling acid solution (typically 3:1 v/v ratio of HCl:HNO_3 at 100 °C for 4 h). UV–vis DRS measurements of each sample were conducted by using Shimadzu UV-3600 Plus equipped with Fourier transform infrared spectrophotometer IRTracer-100. BET specific surface area of the engineered nanomaterials was analysed using BET spectrometer (Micromeritics ASAP 2460 Surface Area and Porosity Analyzer) by N_2 adsorption isotherm at liquid nitrogen temperature (77 K). Before BET measurement, the sample was degassed at 110 °C over 15 h under nitrogen flow using the sample degas system (Micrometritics FlowPrep 060).

Sorption experiments

Batch adsorption experiments were performed to assess the PFAS sorption performance of the plasmonic photocatalysts. Fifteen-millilitre tubes were prepared each with approximately 20 mg particles (MSN–NH_2–Pd and MSN–NH_2–Pt) for the sorption experiment. Ten-millilitre solutions of 1–500 ppm PFAS were prepared, with 1,000 ppm stock solutions and DI water bubbled with CO_2 to control pH, then added to each tube. Batch experiments were mixed on a rotating shaker for 24 h (in the dark) to achieve equilibrium; solution pH was measured at the start and end of the experiment. After each 24 h, 1.5-ml samples were taken and centrifuged. The supernatant was then sampled, diluted to achieve the relevant instrument concentration range, and analysed with a Shimadzu Scientific Instruments 8060 Triple-Quad LC–MS system. Duplicate experiments were conducted, including blanks without plasmonic photocatalyst particles, for comparison and sorption capacity calculations at each equilibrium concentration. Equilibrium data (in aqueous and solid phases) were plotted, and Langmuir and Freundlich sorption models were assessed for each isotherm; for Freundlich isotherms, model fits were performed for the range below the maximum sorption capacity (approximated using the average of sorption capacity values at a maximum steady state). In addition to other isotherm parameters, maximum sorption capacity and half-saturation concentrations were calculated for each model fit. Corresponding equations for Langmuir (equation (5)) and Freundlich (equation (6)) isotherms are given below.

$$q_e = \frac{q_{max} b C_e}{1 + b C_e} \tag{5}$$

$$q_e = K_f C_e^{\ n} \tag{6}$$

where q_e is the amount of contaminant adsorbed per gram of sorbent at equilibrium (mg g^{-1}), C_e is the equilibrium concentration of the contaminant in solution (mg l^{-1} or ppm), q_{max} is the maximum adsorption capacity (mg g^{-1}) and b is the Langmuir constant related to adsorption affinity (l mg^{-1}) in the Langmuir isotherm (equation (5)); and K_f is the Freundlich constant indicative of adsorption capacity ((mg g^{-1}) (l $mg^{-1})^n$), and n is the adsorption intensity (unitless) in the Freundlich isotherm (equation (6)).

Photocatalytic reactions

Photocatalytic experiments were conducted under constant UV irradiation at 254 nm (UVC, Phillips, low-pressure mercury lamps, light intensity of 2.6 mW cm^{-2}) or 368 nm (UVA, USHIO, phosphor-coated low-pressure mercury lamps, light intensity of 7.3 mW cm^{-2}) in a 100-ml quartz vial. The reaction suspension consisted of 400 mg l^{-1} (ppm) of catalyst, 10 mg l^{-1} (ppm) of PFOA and 2.5 ml of MeOH. Before UV irradiation, the quartz vial containing reaction suspension was sealed and bubbled with CO_2 (and H_2, if necessary) for 30 min. The working pH was maintained in the range of 4.2–4.5 with the use of CO_2 bubbling before each experiment. Samples were collected at different reaction times (hourly for the first 4 h and then every 2 h until the eighth hour) and analysed accordingly for PFAS and F^- concentration. In the case of long-term experiments (up to 5 days) under constant UVA irradiation, sampling started at 24 h and was performed at 12-h intervals thereafter. The concentration of PFAS and corresponding by-products were measured using LC–MS (Shimadzu LCMS TQ 8060) while the F^- concentration was determined by IC. The concentrations of PFOA and catalyst were kept constant in each scavenger experiment. Carbonate–bicarbonate buffer was used as the weak basic buffer in the pH study. For scavenger experiments, 2.5 ml TBA, 2.5 ml IPA,

400 mg $AgNO_3$, 100 mg SOD and 100 mg EDTA were used. Reaction constants associated with stated scavengers can be given as $k_{AgNO_3,e_{aq}^-} = 2.8 \times 10^9\ M^{-1}\ s^{-1}$, $k_{AgNO_3,OH} = 1.0 \times 10^{10}\ M^{-1}\ s^{-1}$ (ref. 52), $k_{SOD,O_2^{\bullet-}} = \sim 2 \times 10^9\ M^{-1}\ s^{-1}$, $k_{SOD,OH} = \sim 1.0 \times 10^{10}\ M^{-1}\ s^{-1}$) (ref. 64) and $k_{EDTA,h^+} = 8.6 \times 10^9\ M^{-1}\ s^{-1}$ (ref. 65). Photon flux, the number of photons incident per unit area per unit time, was calculated based on light intensity and wavelength to evaluate the availability of photons for catalytic processes. The resulting photon flux values were used to normalize reaction rates for direct comparison between different light irradiation (UVA and UVC) efficiencies; full equations and calculation details are provided in the Results and Discussion section of the SI.

IC measurements

IC was used to measure F^- concentration with a Metrohm 940 Professional IC Vario equipped with a Metrohm 919 autosampler and Metrosep A Supp 5–150/4.0 anion column. The F^- concentration in the supernatant was measured, and the percentage of defluorination was calculated based on the theoretical initial F^- concentration, which was determined from the initial PFAS concentrations obtained through LC-MS measurements. The calculation is provided in Eq. 7 below[30].

$$\text{Overall deF\%} = \frac{[F^-]}{[\text{PFAS}]_0 \times N_{C\text{-}F}} \times 100 \quad (7)$$

where $[F^-]$ corresponds to the fluoride molar concentration measured using IC, $[PFOA]_0$ corresponds to the initial PFAS molar concentration measured using LC-MS, and N_{C-F} corresponds to the number of C–F bond exits in the structure of the used PFAS molecule.

^{19}F NMR analysis

NMR samples were prepared by sampling the reaction at delineated times, transferring 500 µl aliquots to new NMR tubes, and adding 10% D_2O to the NMR tube (for NMR deuterium lock). NMR spectra were recorded on an Agilent DD2 400 MHz spectrometer equipped with a OneNMR probe at 23 °C. Standard Agilent pulse sequences were employed. ^{19}F NMR spectra are reported in ppm. A spectral window with a range of -50 to -250 ppm was used. Following preliminary NMR scans, the 72 h samples were acidified (10 µl of 0.1 M HNO_3 were added to each NMR tube) to transform aqueous F^- into HF ($pK_a \approx 3.2$). The parameters of NMR analysis are outlined in Supplementary Table 1. All ^{19}F NMR spectra processing was completed using MestreNova software. A detailed description of the methodology for referencing ^{19}F NMR spectra is provided in the 'Results' and 'Discussion' sections of Supplementary Information, and identified chemical shifts are tabulated in Supplementary Table 2.

Quantitative LC–MS measurements

Mass spectrometric measurements were performed with a Shimadzu Scientific Instruments 8060 Triple-Quad LC–MS system, equipped with a Nexera LC-40D xs UHPLC, consisting of a CBM-40 Lite system controller, a DGU-405 Degasser Unit, two LC-40D XS UHPLC pumps, a SIL-40C XS autosampler and a Column Oven CTO-40S. Mass spectra were subsequently recorded with the triple quadrupole (TQ) 8060 mass spectrometer. The samples were held at 20 °C in the autosampler compartment after ultrasonification. One microlitre of each sample was injected into a sample loop and separated on a Shimadzu Velox PFPP column, 1.8 µl, 2.1 × 100 mm, equilibrated at 40 °C in a column oven. A binary gradient was used during the measurements, respectively, solvent A (Water, HPLC grade Chromasolv, with 0.1% Formic Acid) and solvent B (MeOH, HPLC grade Chromasolv).

HR-MS analysis

HR-MS measurements were conducted using a Shimadzu Scientific Instruments QToF 9030 LC–MS system, equipped with a Nexera LC-40D xs UHPLC set-up identical to the one used in the quantitative LC–MS analysis. For mass spectrum recording, the quadrupole time-of-flight (QToF) 9030 mass spectrometer was employed. Samples were maintained at 4 °C within the autosampler compartment. A 1-µl aliquot of each sample was injected into a sample loop and separated using a Shimadzu Velox PFPP column (1.8 µm, 2.1 × 100 mm), equilibrated at 40 °C in a column oven. A binary gradient was applied with solvent A being water (HPLC grade Chromasolv) with 0.1% formic acid and solvent B being acetonitrile (HPLC grade Chromasolv) with no additives. The flow rate was set at 0.250 ml min^{-1}, and the gradient composition varied as follows: from 0 to 2 min, 60% A and 40% B; from 2 to 6.5 min, 15% A and 85% B; from 6.5 to 7.5 min, 15% A and 85% B; from 7.5 to 7.51 min, 60% A and 40% B; and from 7.51 to 10 min, 60% A and 40% B. The ionization source operated in electrospray ionization mode with the electrospray needle at −3.0 kV. Nebulizer gas was set at 2 l min^{-1}, heating gas flow at 10 l min^{-1} and the interface at 300 °C. Dry gas was maintained at 10 l min^{-1}, with the desolvation line at 250 °C and the heating block at 400 °C. Mass spectra were acquired in the range of 50–1,000 m/z in negative ion mode, while data-dependent MS/MS fragmentation was performed in the range of 25–500 m/z with a collision energy spread of 40 ± 20 V (CE spread). Measurements and data post-processing were managed using LabSolutions 5.97 Realtime Analysis and PostRun software.

Reporting summary

Further information on research design is available in the Nature Portfolio Reporting Summary linked to this article.

Data availability

The data supporting the findings of this study are available in the article and its Supplementary Information.

References

1. Moody, C. A. & Field, J. A. Perfluorinated surfactants and the environmental implications of their use in fire-fighting foams. *Environ. Sci. Technol.* **34**, 3864–3870 (2000).
2. *Emerging Contaminants—Perfluorooctane Sulfonate (PFOS) and Perfluorooctanoic Acid (PFOA)* (US Environmental Protection Agency, 2014).
3. Moody, C. A. & Field, J. A. Determination of perfluorocarboxylates in groundwater impacted by fire-fighting activity. *Environ. Sci. Technol.* **33**, 2800–2806 (1999).
4. Andrews, D. Q. & Naidenko, O. V. Population-wide exposure to per-and polyfluoroalkyl substances from drinking water in the United States. *Environ. Sci. Technol. Lett.* **7**, 931–936 (2020).
5. U.S. Environmental Protection Agency Designation of perfluorooctanoic acid (PFOA) and perfluorooctanesulfonic acid (PFOS) as CERCLA hazardous substances. *Fed. Regist.* **89**, 38796–38839 (2024).
6. Wanninayake, D. M. Comparison of currently available PFAS remediation technologies in water: a review. *J. Environ. Manage.* **283**, 111977 (2021).
7. Ross, I. et al. A review of emerging technologies for remediation of PFASs. *Remediation J.* **28**, 101–126 (2018).
8. Maldonado, V. in *Green Chemistry: Water and Its Treatment* (eds Benvenuto, M. A. & Plaumann, H.) 133–148 (De Gruyter, 2021).
9. O'Connor, J. et al. Distribution, transformation and remediation of poly- and per-fluoroalkyl substances (PFAS) in wastewater sources. *Process Saf. Environ. Prot.* **164**, 91–108 (2022).
10. Glass, S. et al. Merits, limitations and innovation priorities for heterogeneous catalytic platforms to destroy PFAS. *Nat. Water* **3**, 644–654 (2025).
11. MacIsaac, S. A. et al. UV LED wastewater disinfection: the future is upon us. *Water Res. X* **24**, 100236 (2024).
12. Pelayo, D., Rivero, M. J., Santos, G., Gómez, P. & Ortiz, I. Techno-economic evaluation of UV light technologies in water remediation. *Sci. Total Environ.* **868**, 161376 (2023).

13. Liu, C. J. et al. Pilot-scale field demonstration of a hybrid nanofiltration and UV-sulfite treatment train for groundwater contaminated by per- and polyfluoroalkyl substances (PFASs). *Water Res.* **205**, 117677 (2021).
14. Dong, Y., Hu, C., Xiong, H., Long, R. & Xiong, Y. Plasmonic catalysis: new opportunity for selective chemical bond evolution. *ACS Catal.* **13**, 6730–6743 (2023).
15. Campos, A. et al. Plasmonic quantum size effects in silver nanoparticles are dominated by interfaces and local environments. *Nat. Phys.* **15**, 275–280 (2019).
16. Zhao, J., Xue, S., Ji, R., Li, B. & Li, J. Localized surface plasmon resonance for enhanced electrocatalysis. *Chem. Soc. Rev.* **50**, 12070–12097 (2021).
17. Kung, P.-Y., Pan, F. & Su, Y.-H. Spintronic hydrogen evolution induced by surface plasmon of silver nanoparticles loaded on Fe- and Co-doped ZnO nanorods. *J. Mater. Chem. A* **9**, 24863–24873 (2021).
18. Li, H., Wang, S., Chi, H. & Li, C. Photocatalytic water splitting driven by surface plasmon resonance. *ChemPhotoChem* **8**, e202300049 (2023).
19. Hou, W. & Cronin, S. B. A review of surface plasmon resonance-enhanced photocatalysis. *Adv. Funct. Mater.* **23**, 1612–1619 (2013).
20. Gellé, A. et al. Applications of plasmon-enhanced nanocatalysis to organic transformations. *Chem. Rev.* **120**, 986–1041 (2020).
21. Zhou, L. et al. Quantifying hot carrier and thermal contributions in plasmonic photocatalysis. *Science* **362**, 69–72 (2018).
22. Schrama, F. R. A. et al. Light-driven interfaces for PFAS detection and destruction. *RSC Appl. Interfaces* **1**, 833–845 (2024).
23. Nayak, S. K., Bhardwaj, K., Verma, P. K. & Yamijala, S. S. R. K. C. Plasmon-induced degradation of short-chain PFAS by noble metal nanoclusters. *J. Phys. Chem. Lett.* **16**, 8046–8055 (2025).
24. Kankala, R. K. et al. Nanoarchitectured structure and surface biofunctionality of mesoporous silica nanoparticles. *Adv. Mater.* **32**, 1907035 (2020).
25. Lee, J., Lee, S. S. S., Jung, H., Kim, C. & Fortner, J. D. Precisely controlled bimetallic nanocatalysts on mesoporous silica nanoparticle supports for highly efficient and selective nitrate reduction. *Appl. Catal. B* **361**, 124600 (2025).
26. Gellé, A. & Moores, A. Plasmonic nanoparticles: photocatalysts with a bright future. *Curr. Opin. Green Sustain. Chem.* **15**, 60–66 (2019).
27. Zhang, N. et al. Near-field dielectric scattering promotes optical absorption by platinum nanoparticles. *Nat. Photonics* **10**, 473–482 (2016).
28. Song, Z., Tang, H., Wang, N. & Zhu, L. Reductive defluorination of perfluorooctanoic acid by hydrated electrons in a sulfite-mediated UV photochemical system. *J. Hazard. Mater.* **262**, 332–338 (2013).
29. Bentel, M. J. et al. Defluorination of per- and polyfluoroalkyl substances (PFASs) with hydrated electrons: structural dependence and implications to PFAS remediation and management. *Environ. Sci. Technol.* **53**, 3718–3728 (2019).
30. Wen, Y. et al. Integrated photocatalytic reduction and oxidation of perfluorooctanoic acid by metal–organic frameworks: key insights into the degradation mechanisms. *J. Am. Chem. Soc.* **144**, 11840–11850 (2022).
31. Sun, Z. et al. UV/nitrilotriacetic acid process as a novel strategy for efficient photoreductive degradation of perfluorooctanesulfonate. *Environ. Sci. Technol.* **52**, 2953–2962 (2018).
32. Tian, H., Gao, J., Li, H., Boyd, S. A. & Gu, C. Complete defluorination of perfluorinated compounds by hydrated electrons generated from 3-indole-acetic-acid in organomodified montmorillonite. *Sci. Rep.* **6**, 32949 (2016).
33. Liu, Z. et al. Near-quantitative defluorination of perfluorinated and fluorotelomer carboxylates and sulfonates with integrated oxidation and reduction. *Environ. Sci. Technol.* **55**, 7052–7062 (2021).
34. Qu, Y., Zhang, C., Li, F., Chen, J. & Zhou, Q. Photo-reductive defluorination of perfluorooctanoic acid in water. *Water Res.* **44**, 2939–2947 (2010).
35. Long, M. et al. Adsorption and reductive defluorination of perfluorooctanoic acid over palladium nanoparticles. *Environ. Sci. Technol.* **55**, 14836–14843 (2021).
36. Smaili, H. & Ng, C. Adsorption as a remediation technology for short-chain per- and polyfluoroalkyl substances (PFAS) from water—a critical review. *Environ. Sci. Water Res. Technol.* **9**, 344–362 (2023).
37. Gu, Y., Dong, W., Luo, C. & Liu, T. Efficient reductive decomposition of perfluorooctanesulfonate in a high photon flux UV/sulfite system. *Environ. Sci. Technol.* **50**, 10554–10561 (2016).
38. Kannan, U. et al. Short-chain PFAS: a global challenge – environmental fate, health risks, and promising removal technologies. *Results Chem.* **20**, 103000 (2026).
39. Javed, H., Lyu, C., Sun, R., Zhang, D. & Alvarez, P. J. J. Discerning the inefficacy of hydroxyl radicals during perfluorooctanoic acid degradation. *Chemosphere* **247**, 125883 (2020).
40. Javed, H. et al. Discerning the relevance of superoxide in PFOA degradation. *Environ. Sci. Technol. Lett.* **7**, 653–658 (2020).
41. Banayan Esfahani, E., Asadi Zeidabadi, F., Zhang, S. & Mohseni, M. Photo-chemical/catalytic oxidative/reductive decomposition of per- and poly-fluoroalkyl substances (PFAS), decomposition mechanisms and effects of key factors: a review. *Environ. Sci. Water Res. Technol.* **8**, 698–728 (2022).
42. Cui, J., Gao, P. & Deng, Y. Destruction of per- and polyfluoroalkyl substances (PFAS) with advanced reduction processes (ARPs): a critical review. *Environ. Sci. Technol.* **54**, 3752–3766 (2020).
43. Lei, X. et al. A review of PFAS adsorption from aqueous solutions: current approaches, engineering applications, challenges, and opportunities. *Environ. Pollut.* **321**, 121138 (2023).
44. Amano, H. et al. The 2020 UV emitter roadmap. *J. Phys. D* **53**, 503001 (2020).
45. da Silva, A. G. M., Rodrigues, T. S., Wang, J. & Camargo, P. H. C. Plasmonic catalysis with designer nanoparticles. *Chem. Commun.* **58**, 2055–2074 (2022).
46. Langhammer, C., Yuan, Z., Zorić, I. & Kasemo, B. Plasmonic properties of supported Pt and Pd nanostructures. *Nano Lett.* **6**, 833–838 (2006).
47. Chen, Z. et al. Amine-functionalized A-center sphalerite for selective and efficient destruction of perfluorooctanoic acid. *Environ. Sci. Technol.* **57**, 10438–10447 (2023).
48. Wang, J., Cao, C., Zhang, Y., Zhang, Y. & Zhu, L. Underneath mechanisms into the super effective degradation of PFOA by BiOF nanosheets with tunable oxygen vacancies on exposed (101) facets. *Appl. Catal. B* **286**, 119911 (2021).
49. Soroushian, B., Lampre, I., Belloni, J. & Mostafavi, M. Radiolysis of silver ion solutions in ethylene glycol: solvated electron and radical scavenging yields. *Radiation Physics and Chemistry* **72**, 111–118 (2005).
50. Jeon, T. H. et al. Ag(I) ions working as a hole-transfer mediator in photoelectrocatalytic water oxidation on WO_3 film. *Nat. Commun.* **11**, 967 (2020).
51. Solti, D. et al. Plasmon-generated solvated electrons for chemical transformations. *J. Am. Chem. Soc.* **144**, 20183–20189 (2022).
52. Buxton, G. V., Greenstock, C. L., Helman, W. P. & Ross, A. B. Critical review of rate constants for reactions of hydrated electrons, hydrogen atoms and hydroxyl radicals (·OH/·O^- in aqueous solution. *J. Phys. Chem. Ref. Data* **17**, 513–886 (1988).

53. Siefermann, K. R. et al. Binding energies, lifetimes and implications of bulk and interface solvated electrons in water. *Nat. Chem.* **2**, 274–279 (2010).
54. Bockris, J. O. M. & Khan, S. U. M. in *Hydrated Electron in Quantum Electrochemistry* (eds Bockris, J. O. M. & Khan, S. U. M.) Ch. 11, 379–420 (Springer, 1979).
55. Pavliuk, M. V. et al. Hydrated electron generation by excitation of copper localized surface plasmon resonance. *J. Phys. Chem. Lett.* **10**, 1743–1749 (2019).
56. Cabrero-Antonino, J. R., Adam, R., Papa, V. & Beller, M. Homogeneous and heterogeneous catalytic reduction of amides and related compounds using molecular hydrogen. *Nat. Commun.* **11**, 3893 (2020).
57. Li, M., Rasamani, K. D. & Sun, Y. Highly dispersed palladium nanoparticles on silica spheres for photocatalytic hydrodeoxygenation of vanillin. *J. Phys. Chem. C* **125**, 16550–16556 (2021).
58. Luna, A. L. et al. Photocatalytic hydrogen evolution using Ni–Pd/TiO_2: correlation of light absorption, charge-carrier dynamics, and quantum efficiency. *J. Phys. Chem. C* **121**, 14302–14311 (2017).
59. Yamijala, S. S. R. K. C., Shinde, R. & Wong, B. M. Real-time degradation dynamics of hydrated per- and polyfluoroalkyl substances (PFASs) in the presence of excess electrons. *Phys. Chem. Chem. Phys.* **22**, 6804–6808 (2020).
60. Nosaka, Y. & Nosaka, A. Understanding hydroxyl radical (•OH) generation processes in photocatalysis. *ACS Energy Lett.* **1**, 356–359 (2016).
61. Calvillo Solís, J. J. et al. Electrochemical reduction of perfluorooctanoic acid (PFOA): an experimental and theoretical approach. *J. Am. Chem. Soc.* **146**, 10687–10698 (2024).
62. Moller, K., Kobler, J. & Bein, T. Colloidal suspensions of nanometer-sized mesoporous silica. *Adv. Funct. Mater.* **17**, 605–612 (2007).
63. Xu, S., Hartvickson, S. & Zhao, J. X. Increasing surface area of silica nanoparticles with a rough surface. *ACS Appl. Mater. Interfaces* **3**, 1865–1872 (2011).
64. Forman, H. J. & Fridovich, I. Superoxide dismutase: a comparison of rate constants. *Arch. Biochem. Biophys.* **158**, 396–400 (1973).
65. Vel Leitner, N. K., Guilbault, I. & Legube, B. Reactivity of OH and e^-_{aq} from electron beam irradiation of aqueous solutions of EDTA and aminopolycarboxylic acids. *Radiat. Phys. Chem.* **67**, 41–49 (2003).

Acknowledgements

ICP-MS was provided by the Yale Analytical and Stable Isotope Center (YASIC), X-ray diffraction analysis was provided by Yale West Campus Materials Characterization Core (MCC) and TEM was provided by Yale Institute for Nanoscience and Quantum Engineering (YINQ) at Yale University. HR-MS and quantitative LC–MS measurements were performed in the Chemical and Biophysical Instrumentation Center (CBIC) at Yale University (RRID: SCR_021738). Equipment was purchased with funds from Yale University.

Author contributions

O.D.: conceptualization, experimental methodology, data analysis, writing and editing; S.S.S.L.: conceptualization, methodology, data analysis, writing and revising; L.M.W.: experimental methodology and data analysis; S.K.M.: experimental methodology, data analysis and writing; F.M.: experimental methodology, data analysis and writing; C.K.: supervision and reviewing; J.M.M.: resources, mechanistic analysis, reviewing, writing and editing; J.D.F.: supervision, conceptualization, resources, analysis, writing, reviewing and editing.

Funding

This work was supported by 2024 Yale Planetary Solutions Seed Funding and by NIEHS grant nos P42ES023716 and P42ES033815. This work was also supported by the National Research Foundation of Korea (NRF) grant funded by the Korea government (MSIT) (RS-2022-NR071792).

Competing interests

The authors declare no competing interests.

Additional information

Supplementary information The online version contains supplementary material available at https://doi.org/10.1038/s44221-026-00690-1.

Correspondence and requests for materials should be addressed to John D. Fortner.

Peer review information *Nature Water* thanks Sharma Yamijala and the other, anonymous, reviewer(s) for their contribution to the peer review of this work.

Reprints and permissions information is available at www.nature.com/reprints.

Publisher's note Springer Nature remains neutral with regard to jurisdictional claims in published maps and institutional affiliations.

Open Access This article is licensed under a Creative Commons Attribution-NonCommercial-NoDerivatives 4.0 International License, which permits any non-commercial use, sharing, distribution and reproduction in any medium or format, as long as you give appropriate credit to the original author(s) and the source, provide a link to the Creative Commons licence, and indicate if you modified the licensed material. You do not have permission under this licence to share adapted material derived from this article or parts of it. The images or other third party material in this article are included in the article's Creative Commons licence, unless indicated otherwise in a credit line to the material. If material is not included in the article's Creative Commons licence and your intended use is not permitted by statutory regulation or exceeds the permitted use, you will need to obtain permission directly from the copyright holder. To view a copy of this licence, visit http://creativecommons.org/licenses/by-nc-nd/4.0/.

© The Author(s) 2026

nature portfolio

Corresponding author(s): John D. Fortner

Last updated by author(s): 12/5/2025

Reporting Summary

Nature Portfolio wishes to improve the reproducibility of the work that we publish. This form provides structure for consistency and transparency in reporting. For further information on Nature Portfolio policies, see our Editorial Policies and the Editorial Policy Checklist.

Statistics

For all statistical analyses, confirm that the following items are present in the figure legend, table legend, main text, or Methods section.

n/a	Confirmed
☐	☒ The exact sample size (*n*) for each experimental group/condition, given as a discrete number and unit of measurement
☐	☒ A statement on whether measurements were taken from distinct samples or whether the same sample was measured repeatedly
☒	☐ The statistical test(s) used AND whether they are one- or two-sided *Only common tests should be described solely by name; describe more complex techniques in the Methods section.*
☒	☐ A description of all covariates tested
☒	☐ A description of any assumptions or corrections, such as tests of normality and adjustment for multiple comparisons
☐	☒ A full description of the statistical parameters including central tendency (e.g. means) or other basic estimates (e.g. regression coefficient) AND variation (e.g. standard deviation) or associated estimates of uncertainty (e.g. confidence intervals)
☒	☐ For null hypothesis testing, the test statistic (e.g. *F*, *t*, *r*) with confidence intervals, effect sizes, degrees of freedom and *P* value noted *Give P values as exact values whenever suitable.*
☒	☐ For Bayesian analysis, information on the choice of priors and Markov chain Monte Carlo settings
☒	☐ For hierarchical and complex designs, identification of the appropriate level for tests and full reporting of outcomes
☒	☐ Estimates of effect sizes (e.g. Cohen's *d*, Pearson's *r*), indicating how they were calculated

Our web collection on statistics for biologists contains articles on many of the points above.

Software and code

Policy information about availability of computer code

Data collection	N/A
Data analysis	N/A

For manuscripts utilizing custom algorithms or software that are central to the research but not yet described in published literature, software must be made available to editors and reviewers. We strongly encourage code deposition in a community repository (e.g. GitHub). See the Nature Portfolio guidelines for submitting code & software for further information.

Data

Policy information about availability of data

All manuscripts must include a data availability statement. This statement should provide the following information, where applicable:

- Accession codes, unique identifiers, or web links for publicly available datasets
- A description of any restrictions on data availability
- For clinical datasets or third party data, please ensure that the statement adheres to our policy

Available upon request.

Research involving human participants, their data, or biological material

Policy information about studies with human participants or human data. See also policy information about sex, gender (identity/presentation), and sexual orientation and race, ethnicity and racism.

Reporting on sex and gender	N/A
Reporting on race, ethnicity, or other socially relevant groupings	N/A
Population characteristics	N/A
Recruitment	N/A
Ethics oversight	N/A

Note that full information on the approval of the study protocol must also be provided in the manuscript.

Field-specific reporting

Please select the one below that is the best fit for your research. If you are not sure, read the appropriate sections before making your selection.

☐ Life sciences ☐ Behavioural & social sciences ☒ Ecological, evolutionary & environmental sciences

For a reference copy of the document with all sections, see nature.com/documents/nr-reporting-summary-flat.pdf

Ecological, evolutionary & environmental sciences study design

All studies must disclose on these points even when the disclosure is negative.

Study description	Photo-driven, plasmon-enhanced catalysis enables high-efficiency PFAS degradation in water under ambient conditions. UV-induced localized surface plasmon resonance (LSPR) catalyzes complete reductive defluorination of perfluorooctanoic acid (PFOA) and perfluorooctane sulfonic acid (PFOS), two legacy contaminants. Stable, quantum-sized palladium and platinum nanocatalysts supported on aminated mesoporous silica nanoparticles (MSN-NH2-Pd and MSN-NH2-Pt) rapidly transform PFOA and PFOS, with, or near, 100% stoichiometric defluorination under low-intensity UVC or UVA irradiation at room temperature. Time-resolved 19F NMR and high-resolution mass spectrometry, among other analyses, reveal a stepwise reductive hydrodefluorination pathway that proceeds without the formation of short-chain products, a major process advantage. Mechanistic studies identify hydrated electrons and in situ hydrogen generation as key reactive species, confirmed by scavenger and control experiments. Taken together, the approach harnesses synergistic interfacial PFAS sorption, plasmon-induced hydrogen evolution, and hydrated electron formation to enable a low-energy, scalable platform for sustainable PFAS treatment via complete defluorination.
Research sample	Water and material samples.
Sampling strategy	Experiments were done in triplicate and reactions were sampled over time.
Data collection	Researcher collected data through standard procedures.
Timing and spatial scale	No spatial scale is applicable for catalyst characterization. Reactions were sampled over the course of minutes to days as needed.
Data exclusions	None
Reproducibility	All experiments were performed in triplicate.
Randomization	N/A
Blinding	N/A

Did the study involve field work? ☐ Yes ☒ No

Reporting for specific materials, systems and methods

We require information from authors about some types of materials, experimental systems and methods used in many studies. Here, indicate whether each material, system or method listed is relevant to your study. If you are not sure if a list item applies to your research, read the appropriate section before selecting a response.

Materials & experimental systems

n/a	Involved in the study
☒	☐ Antibodies
☒	☐ Eukaryotic cell lines
☒	☐ Palaeontology and archaeology
☒	☐ Animals and other organisms
☒	☐ Clinical data
☒	☐ Dual use research of concern
☒	☐ Plants

Methods

n/a	Involved in the study
☒	☐ ChIP-seq
☒	☐ Flow cytometry
☒	☐ MRI-based neuroimaging

Plants

Seed stocks	N/A
Novel plant genotypes	N/A
Authentication	N/A